

pubs.acs.org/journal/apchd5 Article

# Transport and Spatial Separation of Valley Coherence via Few Layer WS<sub>2</sub> Exciton—Polaritons

Chawina De-Eknamkul, Wenzhuo Huang, Xingwang Zhang, Yundong Ren, and Ertugrul Cubukcu\*



Cite This: ACS Photonics 2024, 11, 1078-1084



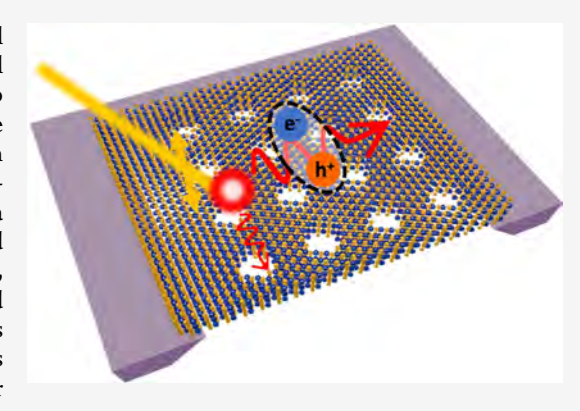
**ACCESS** I

III Metrics & More

Article Recommendations

s Supporting Information

ABSTRACT: The optical response in two-dimensional transition-metal dichalcogenides (2D TMDCs) is dominated by excitons. The lack of spatial inversion symmetry in the hexagonal lattice within each TMDC layer leads to valley-dependent excitonic emission of photoluminescence. Here, we demonstrate experimentally the spatial separation of valley coherent emission into orthogonal directions through self-resonant exciton polaritons of a free-standing three-layer (3L) WS<sub>2</sub> waveguide. This was achieved by patterning a photonic crystal consisting of a square array of holes, allowing for the far-field probing of valley coherence of engendered exciton—polaritons. Furthermore, we report a detailed experimental modal characterization of this coupled system in good agreement with the theory. Momentum space measurements reveal a degree of valley coherence in the range 30–60%. This work provides a platform for the manipulation of valley excitons in coherent light—matter states for potential implementations of valley—coherent optoelectronics.



KEYWORDS: 2D materials, WS<sub>2</sub>, atomically thin waveguide, directional propagation, guided-mode resonance

# **■ INTRODUCTION**

Excitons engendered in two-dimensional transition-metal dichalcogenides (2D TMDCs) dominate the materials' electromagnetic response in the visible regime as a result of quantum confinement owing to their molecular thickness. 1-3 Upon optical excitation, the quasi-two-dimensional excitons induce large in-plane transition dipoles that can couple strongly with the electromagnetic modes of the system they are in, giving rise to exciton-polaritons with mixed lightmatter character near such resonances.<sup>4,5</sup> This distinct hybridization between TMDC excitons and photon modes brings about unique physical phenomena that are simultaneously photon- and exciton-like, including large propagation distances, long-range coherence, and valley-coherent coupling.6 The study of TMDC exciton-polaritons promises unprecedented ways to confine and control subwavelength light-matter interactions for nanophotonic applications in the visible and near-infrared.

Moreover, 2D excitons in TMDCs with a hexagonal lattice also exhibit unique valley properties due to a lack of spatial inversion symmetry within each TMDC layer. The dominant direct bandgap of excitons (A-excitons) occurs at two degenerate K and K' valleys in the first Brillouin zone. These two valleys are nonequivalent, as strong spin—orbit coupling in TMDC leads to spin splitting having opposite signs at the K and K' valleys. This strong spin-valley coupling gives rise to a new valley degree of freedom and dipole selection rules, allowing each valley to be populated by either left-

right-handed ( $\sigma^+$  or  $\sigma^-$ ) circularly polarized light.<sup>8</sup> Depending on the intervalley scattering dynamics and exciton lifetime, the emitted photoluminescence (PL) can bear a large degree of circular polarization, with two-layer and three-layer WS<sub>2</sub> exhibiting as high as 60 and 90% at room temperature, respectively. 10-12 More interestingly, several works showed that TMDC excitons also display a degree of valley coherence. 10,13,14 In this case, the linear polarization of the excitation source is preserved in the coherent superposition of K and K' valley-polarized excitons, and the resulting PL emission possesses a preferred direction of linear polarization corresponding to that of the excitation source. Several groups have successfully created chiral interfaces capable of spatially separating excitons based on their valley polarization, creating a pathway to utilize the valley degree of freedom for information storage and processing. 15-17

Embedding TMDCs in a photonic cavity has been shown to produce valley-polarized cavity exciton—polaritons, drawing great interest in the manipulation of valley polarization in coherent light and matter states. 8,18,19 However, the valley coherence of the in-plane propagating exciton-polaritons has

Received: October 13, 2023 Revised: January 30, 2024 Accepted: February 2, 2024 Published: February 20, 2024





not yet been explored. This is largely due to the fact that exciton-polaritons do not radiate into free space due to momentum mismatch between them, thus prohibiting far-field probing. In our previous work,<sup>20</sup> we overcame this challenge by directly patterning a photonic crystal (PhC) hole array into a suspended WS<sub>2</sub> monolayer to achieve momentum matching. Suspending atomically thin TMDCs in air forms a symmetric waveguide structure and allows the material to support-guided modes confined to the plane of the waveguide with no mode cutoff. In this configuration, the propagating 2D excitonpolariton is transverse electric (TE) polarized, with the electric field polarized in the plane of the material decaying evanescently in the out-of-plane direction. This allowed us to scatter out the dark waveguide modes and experimentally show the existence of the TE waveguide modes in monolayer tungsten disulfide (WS<sub>2</sub>).

Here, we employ this PhC approach to demonstrate room temperature valley-coherent propagation of self-resonant exciton-polaritons in a three-layer (3L) WS<sub>2</sub> waveguide. The PhC hole array patterned directly on a suspended layer of WS<sub>2</sub> acting as a 2D grating provides momentum matching and efficiently couples light in and out of the 2 nm-thick slab waveguide. This allows us to study the dispersion and propagation characteristics of the exciton-polaritons in the form of guided-mode resonances that radiate into free space. We further utilize the large degree of valley polarization and coherence of 3L WS<sub>2</sub> PL to show that the structure can inherently separate linearly polarized exciton-polaritons in space into two perpendicular directions. By analyzing the intensity of the guided-mode resonance emission in the momentum space, we verified that valley coherence is preserved in the propagating exciton-polariton modes.

### RESULTS AND DISCUSSIONS

The atomically thin 3L WS<sub>2</sub> flake was patterned and suspended using a fabrication technique described in our previous work (Supporting Information 1).<sup>20</sup> Figure 1a illustrates a square array of air holes etched into the freestanding 2 nm-thick WS<sub>2</sub> supported by a SiN/Si window. Figure 1b shows a scanning electron micrograph (SEM) of such a suspended 3L WS<sub>2</sub> PhC. Suspending the material in air ensures matching refractive indices on both sides, forming a symmetric waveguide that supports exciton-polariton modes (Supporting Information 2). The hole array introduces out-of-plane scattering losses to the in-plane propagating exciton-polariton modes and allows a small portion of light to couple out of the plane into free space via momentum matching to be detected in the far field. In particular, the introduction of periodic modulation of the refractive index folds the waveguide mode dispersion to the first Brillouin zone, which lies above the light line. <sup>21</sup> The result is a quasi-bound-guided mode resonance characterized by an asymmetric line shape observable in the far field.<sup>22</sup>

The number of layers of the suspended WS<sub>2</sub> was confirmed via PL measurements in Figure 1c. The sample was excited using a 532 nm laser, and the resulting emission spectrum shows two peaks at 630 and 785 nm, corresponding to direct and indirect bandgap transitions, respectively, which are consistent with the emission of 3L WS<sub>2</sub>.<sup>23</sup> The PhC here has a period of 700 nm and a hole diameter of 340 nm. Figure 1d shows the transmission spectrum of the 3L WS<sub>2</sub> PhC at a normal incidence. The spectrum shows two distinct peaks at 624 and 705 nm, corresponding to A-exciton absorption and guided-mode resonance of the PhC, respectively. The

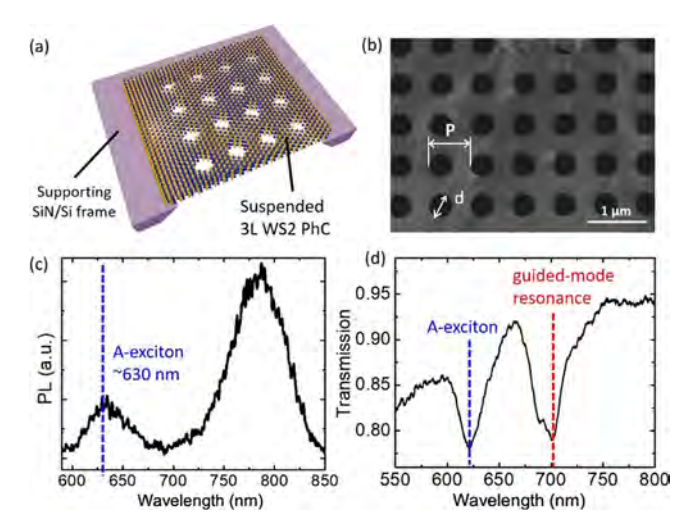


**Figure 1.** Schematic and sample characterization. (a) Schematic of freestanding 3L WS<sub>2</sub> PhC supported by a SiN/Si frame. (b) SEM of the suspended WS<sub>2</sub> PhC. P and d are the period and hole diameter, respectively. (c) PL spectrum of suspended 3L WS<sub>2</sub> excited by using a 532 nm laser. The spectrum shows a direct bandgap excitonic resonance at  $\sim$ 630 nm. An indirect bandgap emission peak close to 800 nm confirms the thickness to be three layers. (d) Transmission spectrum of 3L WS<sub>2</sub> PhC with P=700 nm and d=340 nm. The spectrum shows two resonances at 624 and 705 nm, corresponding to the A-exciton absorption and guided-mode resonance of the PhC, respectively.

suspended atomically thin WS<sub>2</sub> PhC slab exhibits both excitonic absorption resonance and dispersive optical guided-mode resonance, forming a platform for probing the strong interaction between excitons and photons.

A dielectric slab with an array of periodic air holes can be viewed as a modulated waveguide, where the index difference  $\Delta \varepsilon$  determines the strength of modulation. In the case of fewnanometer-thick 3L WS<sub>2</sub> PhC, the modulation is said to be small due to the majority of the mode volume residing in air.<sup>24</sup> Within the weak modulation PhC limit, the locations of the guided-mode resonances reflect the exciton-polariton resonant dispersion in the corresponding unmodulated slab waveguide (i.e., unpatterned WS<sub>2</sub>).<sup>25</sup> The guided exciton—polariton mode has an in-plane propagation constant  $\beta = n_{\text{eff}} k_0$ , where  $n_{\text{eff}}$  is the complex effective mode index, with the imaginary part accounting for both the diffraction and the absorption losses. Using rigorous coupled-wave analysis (RCWA, Supporting Information 3), 26 we derive the momentum matching conditions for the guided-mode resonance in the xy-plane and the in-plane component of the free-space wavevector  $(k_0)$ :

$$(n_{\text{eff}})^2 = \left(\frac{k_x}{k_0} + m \frac{2\pi}{\Lambda k_0}\right)^2 + \left(\frac{k_y}{k_0} + n \frac{2\pi}{\Lambda k_0}\right)^2, m, n$$

$$= 0, 1, 2, \dots$$
(1)

where  $\Lambda$  is the period, and m and n are the order of space harmonic (i.e., diffraction order). From Eq 1, we can see that the guided-mode resonance forms arcs in the momentum

space centered at 
$$\left(-m\frac{2\pi}{\Lambda k_0}, -n\frac{2\pi}{\Lambda k_0}\right)$$
 with a radius of  $n_{\text{eff}}$ 

We first observed the dispersion of exciton—polaritons via angle-resolved transmission measurements using a linearly polarized collimated white light source (Supporting Information 4). In this setup, the sample was mounted on a stage and

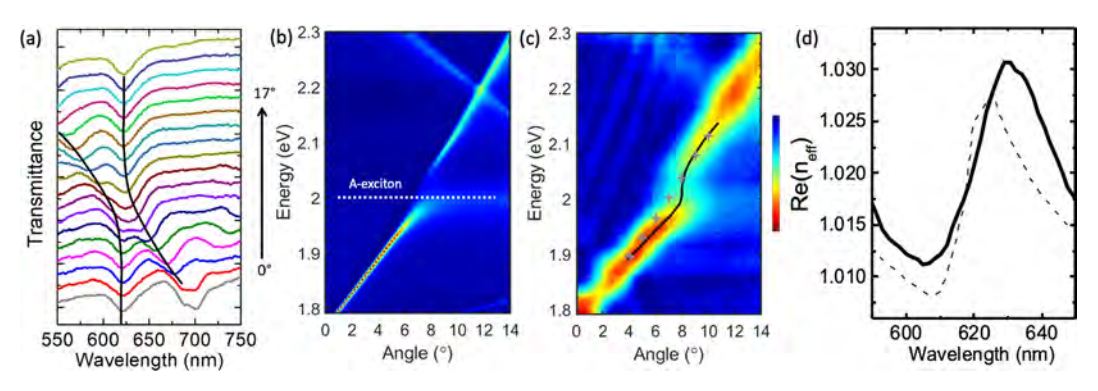


Figure 2. Dispersion of 3L WS<sub>2</sub> PhC guided-mode resonance. (a) Measured transmission spectra at different angles of incidence of the 3L WS<sub>2</sub> PhC. Black curves trace the photonic and excitonic resonances on each spectrum. (b) RCWA calculations of angle-resolved transmission for a 2 nm thick WS<sub>2</sub> PhC with P = 700 nm and d = 340 nm. The data were normalized to unity at each angle. White dotted line represents the A-exciton peak, (c) measured angle-resolved transmission. Data were taken at  $0.2^{\circ}$  incidence intervals and normalized for each angle. Overlaid gray crosses show the dispersion of the same guided-mode resonance of the same PhC made from a material without A exciton for comparison. Black solid line traces the angular position of the exciton–polariton dispersion. (d) Real part of the effective mode index,  $n_{\rm eff}$  is extracted from the dispersion in (b) and (c). Solid and dotted lines show simulated and measured data, respectively.

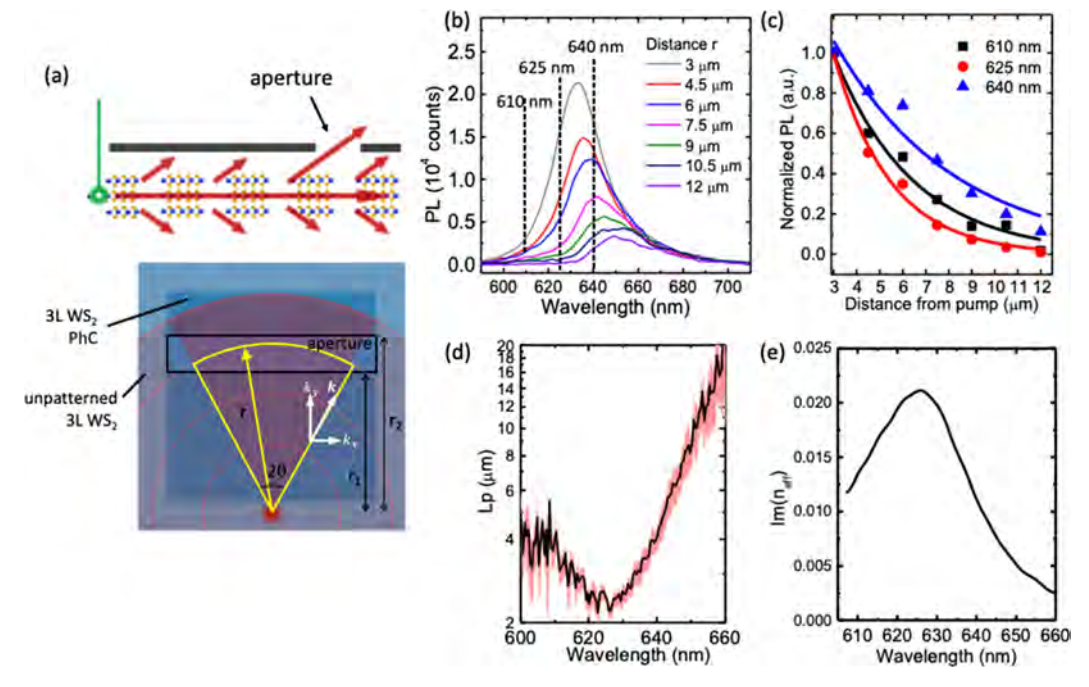
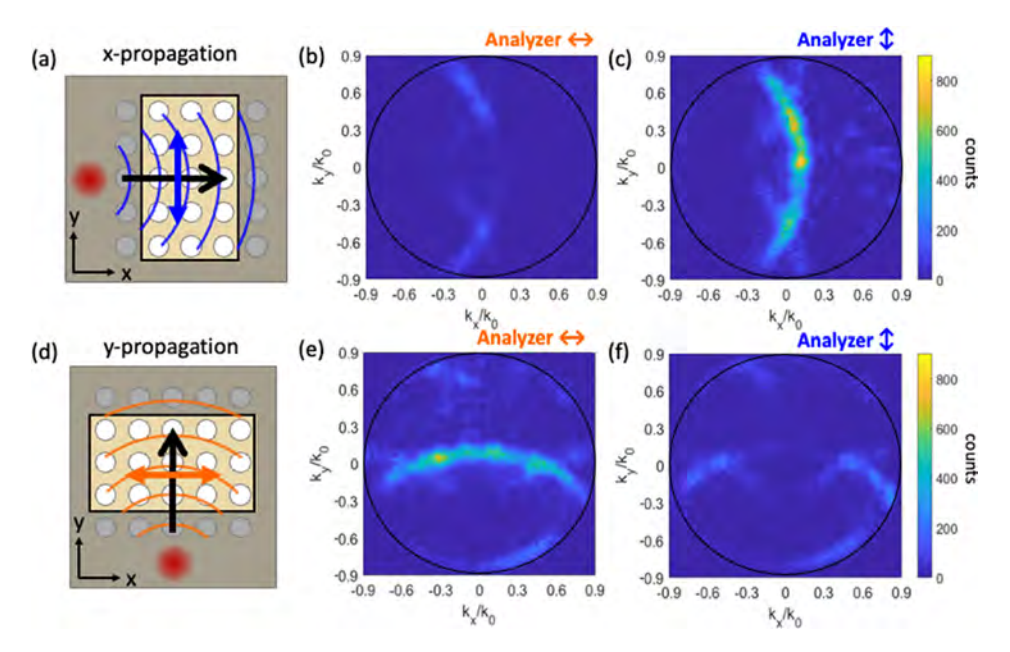


Figure 3. Propagation of exciton—polaritons. (a) Schematic of exciton—polariton propagation experiment. (b) PL spectra measured from a slit at a fixed distance away from the excitation spot. (c) PL intensities at 610, 625, and 640 nm wavelength (vertical dashed lines in (b)) as a function of distance from the excitation spot. The evanescent decay was fitted with the exponential function shown in eq 2. (d) Experimental propagation length  $(L_p)$  of exciton—polariton extracted from PL spectra shown in (b). Red fluctuations show the corresponding fitting error. (e) Imaginary part of the effective mode index extracted from (d).

rotated such that the linear polarization of the source was always in plane with the sample (TE). Figure 2a shows transmission spectra measured at varying angles of incidence from 0° to 17°. The dispersion measurements show the guided-mode resonance blue-shifting toward the exciton resonance at 1.99 eV (~624 nm), as the incident angle increases. When the two resonances approach each other, the dispersion exhibits an anticrossing behavior (black solid line) arising from classical strong coupling between the in-plane excitonic dipoles and the PhC guided-mode resonance. We further analyzed the mode dispersion through RCWA simulations and transmission measurements as shown in Figure 2b,c, respectively. Data in both plots are normalized along all angles at fixed energies. At 8° incidence, the photonic

resonance coincides with the A-exciton resonance. Here, an anomalous dispersion emerges, indicative of classical strong coupling in the WS $_2$  slab. In the presence of losses near the exciton peak, this interaction manifests itself as back bending in the mode dispersion, suggesting that the interaction is in the classical strong coupling regime. We estimated the coupling strength to be  $\sim$ 40 meV. Gray crosses indicate the simulated dispersion of the same photonic mode in a nonexcitonic material for comparison (Supporting Information 4). It is clear that the coupling between excitons and photons leads to a modulated dispersion when the energies of the two modes are degenerate. The exciton and photonic resonance peaks were determined from Figure 2a by fitting two Lorentzian curves over each PL spectrum at a fixed angle.



**Figure 4.** Polarization-dependent propagation of exciton—polariton modes. (a) Schematic of the measurement where propagation in the *x*-direction is observed. (b, c) Measured BFP emission with an *x*- and *y*-polarized analyzer, respectively. (d) Schematic of the measurement, where propagation in the *y*-direction is observed. (e, f) Measured BFP emission with an *x*- and *y*-polarized analyzer, respectively.

Using eq 1 and the measured resonance energies, we extracted the real part of  $n_{\rm eff}$  as shown in Figure 2d.

Next, we directly probed the propagation lengths of exciton-polariton modes in the 3L WS<sub>2</sub> waveguide by using the PL of WS<sub>2</sub> as a near-field light source. To increase the intensity of the direct bandgap exciton, we adopted a laserthinning technique to generate a local emitter with monolayerlike emission in an unpatterned region.<sup>30</sup> The thinning procedure and PL comparison are detailed in Supporting Information 5. We note that this treatment only changed the PL locally on an unpatterned region of the suspended WS<sub>2</sub> PhC, while material properties on the PhC patterned region remained the same. Using this higher quantum efficiency monolayer-like PL as a near-field emitter, we analyzed the evolution of the PL spectra several micrometers away from the excitation spot. The collection system was composed of a 0.9 NA objective, real-space aperture, back focal plane (BFP) lens, and BFP aperture (Supporting Information 6). As illustrated in Figure 3a, an unpatterned area of suspended WS<sub>2</sub> was excited by a focused 532 nm laser with a spot size of approximately 500 nm. At a distance  $r_1$  away from the laser spot, we opened a narrow real-space aperture across the PhC with a slit width of  $\Delta r = r_2 - r_1 \approx 2 \ \mu \text{m}$ . In the BFP, we fixed the aperture to around the middle portion of the arc (eq 1 and Figure S4b) as we increased the distance between the real-space aperture and the excitation spot. Because of the fixed aperture in the BFP (momentum space), only the PL propagated at a certain angle was collected (red area within the slit in Figure 3a). The inplane propagation of the exciton-polariton is approximated as a cylindrical wave whose intensity follows  $\exp(-r/L_p)/r$ , where  $L_{\rm p}$  is the propagation length and r is the distance from the source. The total scattered intensity is proportional to the surface integral of the exciton-polariton intensity, which can be approximated as an exponential function of the distance from the excitation spot for small  $\Delta r$  (Supporting Information 7):

$$I_{\rm BFP} \propto \int_{r_1}^{r_2} \frac{{\rm e}^{-r/L_{\rm p}}}{r} 2\theta r {\rm d}r \approx 2\theta \Delta r {\rm e}^{-r^-/L_{\rm p}}$$
 (2)

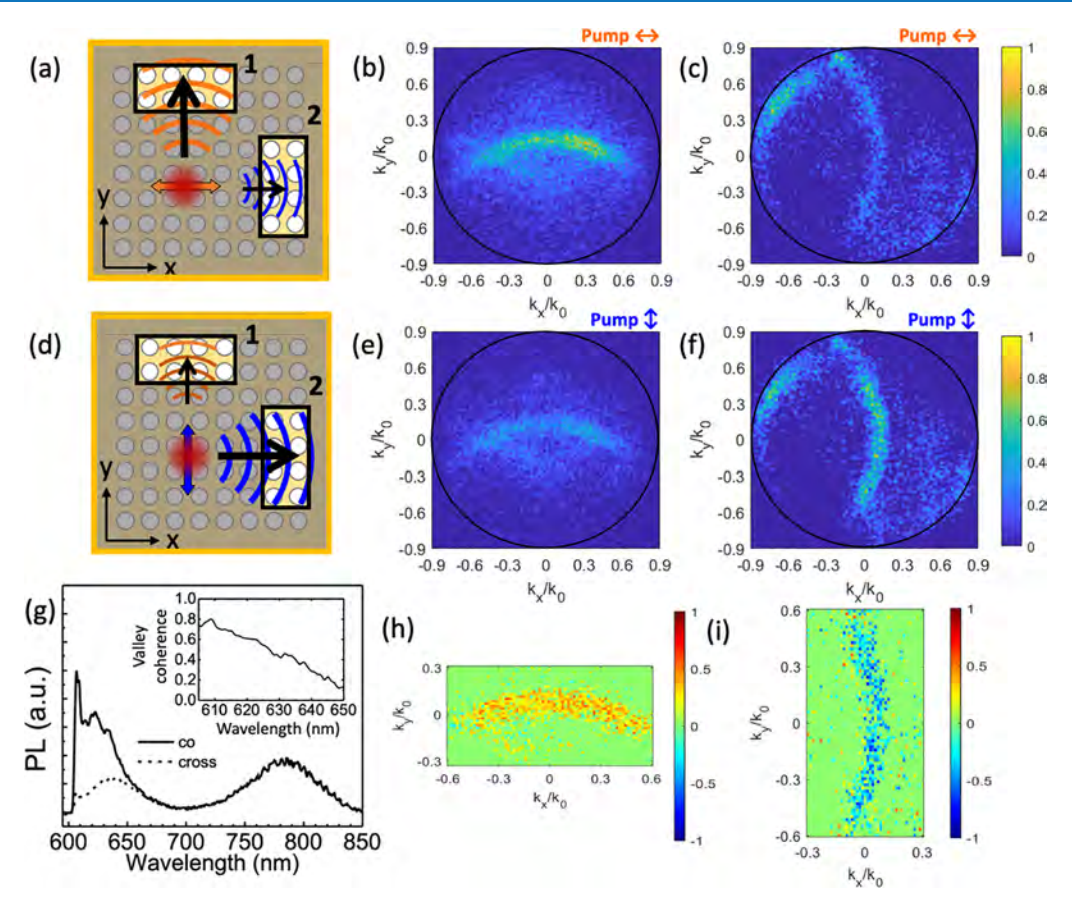
where  $r_1$ ,  $r_2$ , and  $\theta$  are as defined in Figure 3a and  $\overline{r} = (r_1 + r_2)/2$ 

Figure 3b shows the measured PL spectra collected as a function of the distance from the excitation spot. The PL intensity decreases exponentially as the distance increases, with each wavelength exhibiting varying decay constants, which directly relate to the spectral dependence of exciton—polariton propagation length  $L_{\rm p}$  (Figure 3c). By using eq 2 and fitting an exponential decay, we extracted the  $L_{\rm p}$  at each photon energy within the bandwidth of the PL emitter. As seen in Figure 3d,  $L_{\rm p}$  decreases to a minimum ( $\sim\!2~\mu{\rm m}$ ) near the A-exciton energy and increases rapidly as the detuning increases. This trend is consistent with other theoretical and experimental reports on atomically thin TMDC waveguides.  $^{24,32}$  The  $L_{\rm p}$  is directly related to the imaginary part of the propagation constant  $\beta$ :  $^{4,24}$ 

$$L_{\rm p} = \frac{1}{2{\rm Im}(\beta)} \tag{3}$$

Using experimental  $L_{\rm p}$  and eq 3, we obtain the imaginary part of the effective mode index shown in Figure 3e. The plot shows a peak at the A-exciton resonance as absorption loss dominates. The extracted complex effective mode index of the guided-mode resonance (Figure 2d,e) suggests a strong interaction between the slab-guided mode and the WS<sub>2</sub> excitons.

Having established the exciton—polariton dispersion, we continue to examine the polarization characteristics of the guided-mode resonance for manipulation of the valley coherence. The atomically thin  $WS_2$  waveguide is TE in nature, with its electric field polarized in the plane of the material and perpendicular to the direction of propagation. As seen in eq 1, the guided-mode resonance diffracted by the 3L  $WS_2$  PhC forms an arc in the momentum space centered at



**Figure 5.** Transport of exciton—polariton valley coherence. (a, d) Schematic of directional propagation of PL-generated exciton—polaritons when the 594 nm excitation source is *x*-polarized (a) and *y*-polarized (d). (b, e) Measured BFP image of emission from aperture 1 in (a, d) with *x*- and *y*-polarized excitation, respectively. Data were normalized by the maximum intensity counts in (b). (c, f) Measured BFP image for emission from aperture 2 in (a, d) with *x*- and *y*-polarized excitation, respectively. Data were normalized by the maximum counts in (f). (g) Measured PL spectra using an *x*-polarized analyzer of 3L WS<sub>2</sub> at the excitation spot in (a) and (d) obtained using an *x*- (solid line) and *y*-(dashed line) polarized 594 nm pump laser. Subset shows the degree of valley coherence over the A-exciton line width. (h, i) Valley coherence of the exciton—polariton guided-mode resonance in the BFP for emission obtained from apertures 1 (h) and 2 (i).

$$\left(-m\frac{2\pi}{\Lambda k_0}, -n\frac{2\pi}{\Lambda k_0}\right)$$
 with a radius of  $n_{\rm eff}$  and  $\Lambda=700$  nm. Each point on the arc corresponds to the in-plane components,  $k_x$  and  $k_y$ , of the free-space wavevector  $k_0$ , which correlates to the in-plane direction of propagation.

This can be used to resolve the polarization of the quasiguided mode. To this end, we used a polarizer analyzer to extract the x- and y-polarized components of the PhC resonance measured from a slit 4  $\mu$ m away from the linearly polarized excitation spot (Figure 4a,d). For propagation of the generated PL coupled into the exciton-polariton mode in the x-direction (Figure 4a), the diffracted light forms a bright arc in the BFP centered at  $\left(0, -\frac{2\pi}{\Lambda k_0}\right)$ . The dispersion arc in the BFP was obtained through x- and y-polarized analyzers in Figure 4b and c, respectively. Clearly, the y-component of the mode is much stronger, verifying that TE waveguide mode propagating in the x-direction is dominantly y-polarized. The opposite is true for exciton-polariton traveling in the ydirection, as shown in Figure 4e and f. As a control, we rotated the sample and slit by 90° so that we could observe the guidemode resonance emission from the same region of 3L WS<sub>2</sub> PhC in the y-direction. Using the same excitation power and spot, the bright arc is now centered at  $\left(-\frac{2\pi}{\Lambda k_0}, 0\right)$  and the

mode is x-polarized, perpendicular to the direction of propagation. The intensities of the arcs in Figure 4c and e are also comparable, indicating uniform propagation of unpolarized PL in all directions. Slight differences in intensities are attributed to the inherent polarization-dependent bias in the collection path. This polarization-dependent propagation provides a platform for spatial separation of valley—coherent exciton—polaritons.

To this end, we switched to a 594 nm laser to excite the polarized PL emission in 3L WS<sub>2</sub>. The near-resonance excitation results in an exciton peak in the PL spectrum that exhibits a high degree of valley coherence (Supporting Information 9). We moved to the center of the 3L WS<sub>2</sub> PhC and placed two spatial apertures centered 4  $\mu$ m above (aperture 1) and to the right (aperture 2) of the excitation spot, as shown in Figure 5a,d. The BFP arcs were imaged without an analyzer. Valley coherence is defined as  $(I_{\parallel} - I_{\perp})/$  $(I_{\parallel} + I_{\perp})$ , where  $I_{\parallel}$  and  $I_{\perp}$  are the intensities when the polarization of the PL is parallel (co) and perpendicular (cross) to that of the pump, respectively. In Figure 5g, we measured the x-polarized component of the PL emission from the x- and y-polarized 594 nm excitation at the center of the 3L WS<sub>2</sub> PhC. The spectra revealed up to 60% degree of valley coherence over the A-exciton line width (620-650 nm), while the indirect transition exhibits no valley coherence. We note

that the sharp peaks at 607 and 609 nm correspond to the Raman peaks of the  $3L\ WS_2$  exhibiting the same polarization as the pump laser.<sup>33</sup>

When the pump laser is x-polarized (Figure 5a), we observe PL-generated exciton-polariton scattering in the BFP from apertures 1 and 2 (Figure 5b,c, respectively). It is evident that the emission is stronger in aperture 1, indicating that the mode extends primarily in the y-direction when the pump laser is xpolarized. In Figure 5d, the polarization of the pump laser was rotated 90°, and the excitation power was kept constant. Comparing Figure 5e,f, we see that the mode instead expands in the x-direction, as the intensity of the arc is now stronger from aperture 2. We note that as x- and y-polarized components undergo different degrees of attenuation in the collection path of our optical set up. To correct for this, we normalized the BFP measurements by the maximum counts for each aperture. This allows us to directly compare the guidedmode resonance obtained from the two apertures. To evaluate the spatial valley coherence of the guided-mode resonance, we employed the same calculation to the BFP arc intensities for propagation in the x- (aperture 2) and y-direction (aperture 1). Figure 5h,i shows a degree of valley coherence of 30-60% on the BFP arcs for both propagation directions. This is consistent with the valley coherence of the PL at the excitation spot, which suggests the valley coherence of the PL is transferred to the spatial separation of exciton-polariton guided-mode resonance. As a control, we repeated the experiment using optically thin WS<sub>2</sub> as the emitter (Supporting Information 10). We observed similar arc intensities from both apertures independent of the pump polarization. This shows that when the emission is unpolarized or not valley coherent, propagation of exciton-polaritons is nondirectional. Our results show the efficient coupling of valley-coherent exciton-polariton to the TE waveguide mode in atomically thin WS<sub>2</sub>, with the direction of propagation locked to the linear polarization of the exciton polariton.

## CONCLUSIONS

In summary, we demonstrated the directional propagation of valley—coherent exciton—polaritons via guided-mode resonances in a suspended 3L WS $_2$  PhC. Valley coherent PL can be generated by near-resonance excitation preserved via coupling into propagating exciton—polariton modes. Furthermore, the TE-polarized nature of our system can be utilized to spatially separate the valley coherent exciton—polaritons into perpendicular directions. Our unique approach enables the inherent control of valley exciton—polaritons without utilizing an external interface, allowing for high directional coupling efficiency. This work provides a platform for the manipulation of valley excitons in coherent light—matter states for exploring hybrid valley-dependent photonic devices.

## ASSOCIATED CONTENT

#### Supporting Information

The Supporting Information is available free of charge at https://pubs.acs.org/doi/10.1021/acsphotonics.3c01484.

Fabrication details for suspended WS<sub>2</sub> photonic crystal. Transverse electric waveguide modes in an atomically thin symmetric slab waveguide in air. Guided-mode resonances and their effective mode index in a photonic crystal slab. Angle-resolved transmission setup. Dispersion of 3L WS<sub>2</sub> photonic crystal without A-exciton

resonance. Optical thinning procedure of 3L WS<sub>2</sub>. Back focal plane optical set up. Back focal plane arc intensity and calculation of propagation length. Off-resonance and near-resonance excitation of 3L WS<sub>2</sub> photoluminescence. Propagation of unpolarized photoluminescence. Linear polarization resolved photoluminescence spectra and valley coherence of 1L–5L WS<sub>2</sub> (PDF)

#### AUTHOR INFORMATION

#### **Corresponding Author**

Ertugrul Cubukcu — Department of NanoEngineering, University of California, La Jolla, California 92093-0448, United States; Department of Electrical and Computer Engineering, University of California, La Jolla, California 92093-0407, United States; Email: ecubukcu@ucsd.edu

#### **Authors**

Chawina De-Eknamkul — Department of NanoEngineering, University of California, La Jolla, California 92093-0448, United States; orcid.org/0000-0001-7776-9537

Wenzhuo Huang — Department of Electrical and Computer Engineering, University of California, La Jolla, California 92093-0407, United States; orcid.org/0000-0003-2161-3896

Xingwang Zhang — Department of NanoEngineering, University of California, La Jolla, California 92093-0448, United States; Suzhou Institute of Nano-Tech and Nano-Bionics (SINANO), Chinese Academy of Sciences (CAS), Suzhou, Jiangsu 215123, P.R. China; orcid.org/0000-0002-5561-681X

Yundong Ren — Department of NanoEngineering, University of California, La Jolla, California 92093-0448, United States

Complete contact information is available at: https://pubs.acs.org/10.1021/acsphotonics.3c01484

## **Funding**

This work was supported by NSF under the NSF EAGER-Program (ECCS-2139416) and National Institutes of Health, National Eye Institute (1R21EY033676). This work was performed in part at the San Diego Nanotechnology Infrastructure (SDNI) at the University of California, San Diego (UCSD), a member of the National Nanotechnology Coordinated Infrastructure (NNCI), which is supported by the National Science Foundation (ECCS-1542148).

#### **Notes**

The authors declare no competing financial interest.

#### REFERENCES

- (1) Chernikov, A.; Berkelbach, T. C.; Hill, H. M.; Rigosi, A.; Li, Y.; Aslan, B.; Reichman, D. R.; Hybertsen, M. S.; Heinz, T. F. Exciton Binding Energy and Nonhydrogenic Rydberg Series in Monolayer WS<sub>2</sub>. *Phys. Rev. Lett.* **2014**, *113* (7), No. 076802.
- (2) Latini, S.; Olsen, T.; Thygesen, K. S. Excitons in van Der Waals Heterostructures: The Important Role of Dielectric Screening. *Phys. Rev. B* **2015**, 92 (24), No. 245123.
- (3) Butun, S.; Palacios, E.; Cain, J. D.; Liu, Z.; Dravid, V. P.; Aydin, K. Quantifying Plasmon-Enhanced Light Absorption in Monolayer WS<sub>2</sub> Films. ACS Appl. Mater. Interfaces 2017, 9 (17), 15044–15051.
- (4) Alpeggiani, F.; Gong, S. H.; Kuipers, L. Dispersion and Decay Rate of Exciton-Polaritons and Radiative Modes in Transition Metal Dichalcogenide Monolayers. *Phys. Rev. B* **2018**, *97* (20), 1–11.
- (5) Liu, W.; Wang, Y.; Zheng, B.; Hwang, M.; Ji, Z.; Liu, G.; Li, Z.; Sorger, V. J.; Pan, A.; Agarwal, R. Observation and Active Control of a Collective Polariton Mode and Polaritonic Band Gap in Few-Layer

- WS<sub>2</sub> Strongly Coupled with Plasmonic Lattices. *Nano Lett.* **2020**, *20* (1), 790–798.
- (6) Low, T.; Chaves, A.; Caldwell, J. D.; Kumar, A.; Fang, N. X.; Avouris, P.; Heinz, T. F.; Guinea, F.; Martin-Moreno, L.; Koppens, F. Polaritons in Layered Two-Dimensional Materials. *Nat. Mater.* **2017**, 16 (2), 182–194.
- (7) Schaibley, J. R.; Yu, H.; Clark, G.; Rivera, P.; Ross, J. S.; Seyler, K. L.; Yao, W.; Xu, X. Valleytronics in 2D Materials. *Nature Reviews Materials* **2016**, *1*, 11.
- (8) Chen, Y.-J.; Cain, J. D.; Stanev, T. K.; Dravid, V. P.; Stern, N. P. Valley-Polarized Exciton—Polaritons in a Monolayer Semiconductor. *Nature Photon* **2017**, *11* (7), 431–435.
- (9) Mai, C.; Semenov, Y. G.; Barrette, A.; Yu, Y.; Jin, Z.; Cao, L.; Kim, K. W.; Gundogdu, K. Exciton Valley Relaxation in a Single Layer of WS<sub>2</sub> Measured by Ultrafast Spectroscopy. *Phys. Rev. B* **2014**, *90* (4). No. 041414.
- (10) Zhu, B.; Zeng, H.; Dai, J.; Gong, Z.; Cui, X. Anomalously Robust Valley Polarization and Valley Coherence in Bilayer WS<sub>2</sub>. *Proc. Natl. Acad. Sci. U.S.A.* **2014**, *111* (32), 11606–11611.
- (11) Gong, S.-H.; Alpeggiani, F.; Sciacca, B.; Garnett, E. C.; Kuipers, L. Nanoscale Chiral Valley-Photon Interface through Optical Spin-Orbit Coupling. *Science* **2018**, *359* (6374), 443–447.
- (12) Godiksen, R. H.; Wang, S.; Raziman, T. V.; Rivas, J. G.; Curto, A. G. Impact of Indirect Transitions on Valley Polarization in WS<sub>2</sub> and WSe<sub>2</sub>. *Nanoscale* **2022**, *14* (47), 17761–17769.
- (13) Jones, A. M.; Yu, H.; Ghimire, N. J.; Wu, S.; Aivazian, G.; Ross, J. S.; Zhao, B.; Yan, J.; Mandrus, D. G.; Xiao, D.; Yao, W.; Xu, X. Optical Generation of Excitonic Valley Coherence in Monolayer WSe<sub>2</sub>. *Nat. Nanotechnol.* **2013**, *8* (9), 634–638.
- (14) Hao, K.; Moody, G.; Wu, F.; Dass, C. K.; Xu, L.; Chen, C.-H.; Sun, L.; Li, M.-Y.; Li, L.-J.; MacDonald, A. H.; Li, X. Direct Measurement of Exciton Valley Coherence in Monolayer WSe<sub>2</sub>. *Nature Phys.* **2016**, *12* (7), 677–682.
- (15) Sun, L.; Wang, C.-Y.; Krasnok, A.; Choi, J.; Shi, J.; Gomez-Diaz, J. S.; Zepeda, A.; Gwo, S.; Shih, C.-K.; Alù, A.; Li, X. Separation of Valley Excitons in a MoS<sub>2</sub> Monolayer Using a Subwavelength Asymmetric Groove Array. *Nature Photon* **2019**, *13* (3), 180–184.
- (16) Yang, Z.; Aghaeimeibodi, S.; Waks, E. Chiral Light-Matter Interactions Using Spin-Valley States in Transition Metal Dichalcogenides. *Opt. Express* **2019**, *27* (15), 21367.
- (17) Wang, S.; Li, S.; Chervy, T.; Shalabney, A.; Azzini, S.; Orgiu, E.; Hutchison, J. A.; Genet, C.; Samori, P.; Ebbesen, T. W. Coherent Coupling of WS2Monolayers with Metallic Photonic Nanostructures at Room Temperature. *Nano Lett.* **2016**, *16* (7), 4368–4374.
- (18) Liu, X.; Galfsky, T.; Sun, Z.; Xia, F.; Lin, E.; Lee, Y.-H.; Kéna-Cohen, S.; Menon, V. M. Strong Light–Matter Coupling in Two-Dimensional Atomic Crystals. *Nature Photon* **2015**, 9 (1), 30–34.
- (19) Lundt, N.; Dusanowski, Ł.; Sedov, E.; Stepanov, P.; Glazov, M. M.; Klembt, S.; Klaas, M.; Beierlein, J.; Qin, Y.; Tongay, S.; Richard, M.; Kavokin, A. V.; Höfling, S.; Schneider, C. Optical Valley Hall Effect for Highly Valley-Coherent Exciton-Polaritons in an Atomically Thin Semiconductor. *Nat. Nanotechnol.* **2019**, *14* (8), 770–775.
- (20) Zhang, X.; De-Eknamkul, C.; Gu, J.; Boehmke, A. L.; Menon, V. M.; Khurgin, J.; Cubukcu, E. Guiding of Visible Photons at the Ångström Thickness Limit. *Nat. Nanotechnol.* **2019**, *14* (9), 844–850. (21) Fan, S.; Joannopoulos, J. D. Analysis of Guided Resonances in Photonic Crystal Slabs. *Phys. Rev. B* **2002**, *65* (23), No. 235112.
- (22) Zhang, X.; Biekert, N.; Choi, S.; Naylor, C. H.; De-Eknamkul, C.; Huang, W.; Zhang, X.; Zheng, X.; Wang, D.; Johnson, A. T. C.; Cubukcu, E. Dynamic Photochemical and Optoelectronic Control of Photonic Fano Resonances via Monolayer MoS<sub>2</sub> Trions. *Nano Lett.* **2018**, *18* (2), 957–963.
- (23) Zhao, W.; Ghorannevis, Z.; Chu, L.; Toh, M.; Kloc, C.; Tan, P.-H.; Eda, G. Evolution of Electronic Structure in Atomically Thin Sheets of WS<sub>2</sub> and WSe<sub>2</sub>. ACS Nano **2013**, 7 (1), 791–797.
- (24) Khurgin, J. B. Two-Dimensional Exciton—Polariton—Light Guiding by Transition Metal Dichalcogenide Monolayers. *Optica* **2015**, 2 (8), 740.

- (25) Wang, S. S.; Moharam, M. G.; Magnusson, R.; Bagby, J. S. Guided-Mode Resonances in Planar Dielectric-Layer Diffraction Gratings. J. Opt. Soc. Am. A 1990, 7 (8), 1470.
- (26) Wang, S. S.; Magnusson, R. Theory and Applications of Guided-Mode Resonance Filters. *Appl. Opt.* **1993**, 32 (14), 2606.
- (27) Wolff, C.; Busch, K.; Mortensen, N. A. Modal Expansions in Periodic Photonic Systems with Material Loss and Dispersion. *Phys. Rev. B* **2018**, 97 (10), No. 104203.
- (28) Hu, F.; Fei, Z. Recent Progress on Exciton Polaritons in Layered Transition-Metal Dichalcogenides. *Advanced Optical Materials* **2020**, 8 (5), No. 1901003.
- (29) Gonçalves, P. A. D.; Bertelsen, L. P.; Xiao, S.; Mortensen, N. A. Plasmon-Exciton Polaritons in Two-Dimensional Semiconductor/Metal Interfaces. *Phys. Rev. B* **2018**, 97 (4), No. 041402.
- (30) Castellanos-Gomez, A.; Barkelid, M.; Goossens, A. M.; Calado, V. E.; van der Zant, H. S. J.; Steele, G. A. Laser-Thinning of MoS<sub>2</sub>: On Demand Generation of a Single-Layer Semiconductor. *Nano Lett.* **2012**, *12* (6), 3187–3192.
- (31) Hu, F.; Luan, Y.; Scott, M. E.; Yan, J.; Mandrus, D. G.; Xu, X.; Fei, Z. Imaging Exciton—Polariton Transport in MoSe<sub>2</sub> Waveguides. *Nature Photon* **2017**, *11* (6), 356–360.
- (32) Hu, F.; Luan, Y.; Speltz, J.; Zhong, D.; Liu, C. H.; Yan, J.; Mandrus, D. G.; Xu, X.; Fei, Z. Imaging Propagative Exciton Polaritons in Atomically Thin WSe<sub>2</sub> Waveguides. *Phys. Rev. B* **2019**, 100 (12), No. 121301.
- (33) Berkdemir, A.; Gutiérrez, H. R.; Botello-Méndez, A. R.; Perea-López, N.; Elías, A. L.; Chia, C.-I.; Wang, B.; Crespi, V. H.; López-Urías, F.; Charlier, J.-C.; Terrones, H.; Terrones, M. Identification of Individual and Few Layers of WS2 Using Raman Spectroscopy. *Sci. Rep* **2013**, 3 (1), 1755.